Gust mitigation with an oscillating airfoil at low Reynolds number

Cite as: Phys. Fluids **33**, 101905 (2021); https://doi.org/10.1063/5.0065234
Submitted: 30 July 2021 • Accepted: 29 September 2021 • Published Online: 19 October 2021

Naresh Poudel, Meilin Yu and John T. Hrynuk

Physics of Fluids ARTICLE scitation.org/journal/phf

Gust mitigation with an oscillating airfoil at low Reynolds number

Cite as: Phys. Fluids **33**, 101905 (2021); doi: 10.1063/5.0065234
Submitted: 30 July 2021 · Accepted: 29 September 2021 ·
Published Online: 19 October 2021

Naresh Poudel,[1,a] Meilin Yu,[1,b] and John T. Hrynuk[2,c]

AFFILIATIONS

[1]Department of Mechanical Engineering, University of Maryland, Baltimore County, Baltimore, Maryland 21250, USA
[2]DEVCOM—Army Research Lab, Aberdeen Proving Ground, Maryland 21005, USA

Note: This paper is part of the special topic, Tribute to Frank M. White on his 88th Anniversary.
[a]**Electronic mail:** npoudel1@umbc.edu
[b]**Author to whom correspondence should be addressed:** mlyu@umbc.edu
[c]**Electronic mail:** john.t.hrynuk.civ@mail.mil

ABSTRACT

The encounter between micro-aerial vehicles (MAVs) and gusts is often detrimental and mitigating the effects of the gust is important for operating MAVs under severe environmental conditions. This study investigates the impact of vertical gusts on stationary and oscillating NACA0012 (National Advisory Committee for Aeronautics) airfoils at low Reynolds numbers using high-order computational fluid dynamics methods, and identifies key dynamics that dominate gust mitigation. The interaction of the gusts with the stationary airfoil generates large unsteady forces, which exceed the peak static lift coefficient. A simple pitch-down maneuver and oscillating airfoil motion were tested as methods for mitigating the effects of the gusts. A rapid and significant pitch-down maneuver is observed to inadvertently cause a stall event by exceeding the negative stall angle. A stepwise change in the angle of attack (AoA), as the gust develops, is shown to be more effective at mitigating the gust effect. However, this gust mitigation strategy is still not effective if the gust continues to grow in magnitude. Low amplitude wing oscillations were then tested as a novel method for gust mitigation. Increasing the reduced frequency of the oscillating airfoil is shown to dominate the gust and results in a predictable oscillatory lift and drag/thrust behavior. Results also show that this effect is relatively insensitive to variations in the Strouhal number. These results suggest there may be gust mitigation strategies leveraging oscillating wing behaviors on MAVs.

Published by AIP Publishing. https://doi.org/10.1063/5.0065234

I. INTRODUCTION

Due to their small size and low speed, micro-aerial vehicles (MAVs) currently being developed for military surveillance, reconnaissance, and remote sensing missions are prone to encounter flight stability and control issues caused by ambient unsteady flow environments, such as wind gusts. The unsteady loads induced by cross-wind and vertical gusts negatively affect the performance of these vehicles, even severely restricting their operating envelopes. To overcome the negative influence imposed by unsteady gusts, both active and passive flow control strategies, based on *in situ* flow conditions, need to be developed. However, it is challenging to design such control mechanisms for effective gust mitigation. One large obstacle is that the highly transient and nonlinear flow physics in gust-vehicle interaction is still not well understood. In order to improve our understanding of the complex physics behind gust–wing interaction, and to better design future MAVs that can operate in highly unstructured flow environments, this study investigates the impact of gust response on the aerodynamic performance of small-scale wings, and seeks innovative gust mitigation strategies, such as using bio-inspired flapping wing mechanisms.

Flying birds and insects provide excellent examples of MAVs which are capable of alleviating adverse effects from unsteady ambient flows with their flapping wings. However, most studies on flapping wing aerodynamics at low Reynolds numbers have neglected the effect of wind gusts on the aerodynamic performance of flapping wings.[1–6] Küssner[7] and von Karman and Sears[8] pioneered the study of the interaction between a thin airfoil and a sharp edged gust with a small amplitude using the unsteady thin airfoil theory. The studies that followed usually focused on modeling small amplitude transient and oscillating vertical gusts, where a small change in the wing AoA (α) was modeled as a transient lift effect. These methods include Wagner's indicial function and Küssner's function for estimating the lift changes

during a gust encounter. These methods assume low gust ratios (GRs), inviscid flows, and attached flow conditions. While these methods are reflective of large-scale aircraft interacting with updrafts, they do not match the gusts experienced by modern MAVs. Recent work by Smith *et al.*[9] demonstrated a vertical gust in a wind tunnel environment that bears little resemblance to the flow conditions required for traditional gust models, but more closely matched MAV flight environments. Many recent experimental and numerical studies have been carried out to study nonlinear, high magnitude gust–wing interactions.[10–20]

Here, a brief review of some recent work on studying the fundamental response of oscillating airfoils and wings to vertical gusts is presented. The performance of two-dimensional (2D) oscillating airfoils subject to sinusoidal gusts has been studied by Lian and Shyy[11,12] and three-dimensional (3D) flapping wings subject to discrete gusts have been studied by Jones and Yamaleev.[15] It has been shown in these studies that flapping wings can be more resistant to gusts and free-stream turbulence.[15,21] There are also parallel efforts studying the flight performance of flying insects in gusty environments,[21–26] and turbulence conditions.[27–33] Nakata *et al.*[34] showed that flexible flapping wings can be beneficial for longitudinal gust mitigation. Badger *et al.*[35] found that the use of a deflectable tail on a glider model can enhance the stability of Anna's hummingbirds flying into a vertical gust. Jakobi *et al.*[36] studied the effects of gusts impinging from different directions on bumblebees and found that bees can mitigate the gust influence by using different maneuvering strategies. Cheney *et al.*[33] also reported that birds can mitigate gusts through a complex variety of inertial and aerodynamic mechanisms.

Experimental studies on gust–wing interaction are always limited by the methods that researchers have used to generate gusts in the experimental setting. For example, a diffuse vortex generated upstream of test models has commonly been used as a type of gust,[37,38] but this method has some drawbacks. While the generated vortex has diffused before hitting the model, this method can only provide transient up- and down-draft behaviors. Another common gust generation method is to mimic a gust by moving the wing itself, e.g., through a plunge motion.[39] Plunging wings are effective at mimicking a gust, but the extent of the differences between moving-body and moving-fluid gust interactions remains unknown. Tow tank studies[16] produce high quality results but are usually limited in their transient nature, where the wing must keep moving to maintain its forward velocity while it passes through the vertical gust. This limits the ability to create a step-function-like gust, which would simulate a MAV flying into an updraft longer than the vehicle itself. This tow tank gust method has been the most heavily studied in recent years including numerical comparisons. Biler *et al.*[40] performed experimental and computational studies and found that leading edge effective AoA is responsible for the peak lift coefficient, rather than gust ratio or geometric AoA. Badrya *et al.*[41,42] compared the experimental results of Perrotta and Jones[16] and their numerical ones, with a goal of widening the gust in a numerical environment. Their results showed that the maximum lift peak increases with the gust width and asymptotically reaches a stable value, which suggests a longer gust generates a different result when compared to shorter, more transient gusts.

Recently, simple control techniques have been applied to mitigate gust effects. Sedky *et al.*[43,44] used both closed- and open-loop strategies to control the pitch motion to mitigate the gust effect. Andreu Angulo and Babinsky[45,46] used a pitch-down motion control to maintain a zero mean effective AoA during the gust encounter. It should be noted that these experiments in water allowed for response to large magnitude gusts and do not necessarily scale well for air vehicles. In these studies, the duration of the gust acting on the wing is short. The impact of the gust on the wing for a long-duration gust can be significantly different.

The objective of the current study is to investigate potential mechanisms for gust mitigation using pitching-down and oscillating airfoils in a long-lived transverse gust. Unlike previous studies, in which gust–wing interactions are studied over a short range of time, this study investigates long-duration gust–wing interaction based on experiments by Smith *et al.*[9] In this setup, the gust generator creates a vertical gust similar to an updraft that an MAV may encounter in the real world. First, the effects of gusts on a fixed airfoil are documented, followed by an investigation of two gust mitigation strategies: a pitch-down maneuver and wing oscillation motions.

The remainder of this paper is organized as follows. We first introduce the high-order unstructured moving grid-based computational fluid dynamics (CFD) solver in Sec. II and present validation and verification results in Sec. III. After that, we investigate gust–wing interaction over a stationary airfoil in Sec. IV A. We then present the results and discuss the flow physics behind two gust control strategies, a pitch-down maneuver and oscillatory motion, in Secs. IV B and IV C. Section V concludes this study.

II. NUMERICAL METHODS

A. Governing equations

Unsteady compressible Navier–Stokes equations in the conservation form are considered in this study. They can be expressed in the physical domain (t, x, y) as follows:

$$\frac{\partial Q}{\partial t} + \frac{\partial F}{\partial x} + \frac{\partial G}{\partial y} = 0, \tag{1}$$

where $Q = (\rho, \rho u, \rho v, E)^T$ are conservative variables, ρ is the density of fluid, u and v are the x- and y-components of the velocity vector, and E is the total energy given by $E = \frac{p}{\gamma-1} + \frac{1}{2}\rho(u^2 + v^2)$ for a perfect gas in which p is the pressure and γ is the constant specific heat capacity ratio. The total energy formula closes the solution system. F and G are total flux vectors including the inviscid and viscous flux terms in the x- and y-direction, respectively. To facilitate numerical simulation, the governing equation (1) in the physical domain (t, x, y) is transformed into the computational domain (τ, ξ, η) as follows:

$$\frac{\partial \tilde{Q}}{\partial \tau} + \frac{\partial \tilde{F}}{\partial \xi} + \frac{\partial \tilde{G}}{\partial \eta} = 0, \tag{2}$$

where

$$\begin{cases} \tilde{Q} = |J|Q, \\ \tilde{F} = |J|(Q\xi_t + F\xi_x + G\xi_y), \\ \tilde{G} = |J|(Q\eta_t + F\eta_x + G\eta_y). \end{cases} \tag{3}$$

Note that in the coordinate transformation, $\tau = t$ and $(\xi, \eta) \in [-1, 1] \times [-1, 1]$ is a standard element in the computational domain. The Jacobian matrix of the coordinate transformation can be written in the following form:

$$J = \frac{\partial(x, y, t)}{\partial(\xi, \eta, \tau)} = \begin{pmatrix} x_\xi & x_\eta & x_\tau \\ y_\xi & y_\eta & y_\tau \\ 0 & 0 & 1 \end{pmatrix}. \tag{4}$$

The inverse transformation must also exist for a nonsingular transformation. Therefore, the inverse of the Jacobian matrix can be written as

$$J^{-1} = \frac{\partial(\xi, \eta, \tau)}{\partial(x, y, t)} = \begin{pmatrix} \xi_x & \xi_y & \xi_t \\ \eta_x & \eta_y & \eta_t \\ 0 & 0 & 1 \end{pmatrix}. \tag{5}$$

The metrics ξ_t and η_t are related to the grid velocity vector $\vec{v}_{grid}$ as follows:

$$\begin{cases} \xi_t = -\vec{v}_{grid} \cdot \nabla \xi, \\ \eta_t = -\vec{v}_{grid} \cdot \nabla \eta. \end{cases} \tag{6}$$

The geometric conservation law (GCL) has been enforced following the error compensation approach.[47]

B. Spatial discretization and time integration methods

The flux reconstruction/correction procedure via reconstruction (FR/CPR) method[48,49] was used to solve the governing equations. A brief introduction of FR/CPR method is discussed here for the sake of completeness. In FR/CPR methods, the flux terms in Eq. (2) are divided into two parts, i.e., local fluxes $\tilde{F}^{loc}$ constructed from local solutions and correction fluxes $\tilde{F}^{cor}$ by mapping the differences between the local fluxes and the common fluxes on the element interfaces into the entire element with high-order correction functions. This can be expressed as follows:

$$\begin{cases} \tilde{F}(\xi, \eta) = \tilde{F}^{loc}(\xi, \eta) + \tilde{F}^{cor}(\xi, \eta), \\ \tilde{G}(\xi, \eta) = \tilde{G}^{loc}(\xi, \eta) + \tilde{G}^{cor}(\xi, \eta). \end{cases} \tag{7}$$

On substituting Eq. (7) into Eq. (2), the governing equations in the computational domain can be reformulated as

$$\frac{\partial \tilde{Q}}{\partial \tau} + \left(\frac{\partial \tilde{F}^{loc}}{\partial \xi} + \frac{\partial \tilde{G}^{loc}}{\partial \eta} \right) + \left(\frac{\partial \tilde{F}^{cor}}{\partial \xi} + \frac{\partial \tilde{G}^{cor}}{\partial \eta} \right) = 0. \tag{8}$$

In this study, the inviscid common fluxes on the element interfaces were calculated using the Roe approximate Riemann solver[50] and the common viscous fluxes were obtained by the second approach (BR2) developed by Bassi *et al.*[51] To minimize numerical errors when performing simulations on curved elements,[52] Eq. (8) can be transformed back to the physical domain as

$$\frac{\partial Q}{\partial \tau} + \left(\frac{\partial F^{loc}}{\partial \xi} + \frac{\partial G^{loc}}{\partial \eta} \right) + \delta^{cor} - \vec{v}_{grid} \cdot \nabla Q = 0. \tag{9}$$

To solve Eq. (9), it can be rewritten as

$$\frac{\partial Q}{\partial \tau} = R(Q, \nabla Q), \tag{10}$$

and the linearly implicit Rosenbrock–Wanner (ROW) Runge–Kutta method[53] was used for time integration. The general formulation of ROW method is written as follows:

$$\begin{cases} Q^{n+1} = Q^n + \sum_{j=1}^{K} m_j Y_j, \\ \left(\frac{I}{\gamma \Delta t} - \frac{\partial R}{\partial Q} \right)^n Y_i = R\left(Q^n + \sum_{j=1}^{i-1} a_{ij} Y_j \right) \\ \qquad + \frac{1}{\Delta t} \sum_{j=1}^{i-1} c_{ij} Y_j, \quad i = 2, \ldots K. \end{cases} \tag{11}$$

Herein, K is the number of stages; Δt is the time step; and m_j, γ, a_{ij}, and c_{ij} are the coefficients of the ROW scheme. In this study, a third-order accurate spatial discretization and a third-order, four-stage ROW scheme with a time step of 1×10^{-4} were used in all simulations.

C. Dynamic grids deformation

Dynamically deforming grids are needed to accurately model the oscillating wing problems in this study. Herein, the algebraic grid deformation algorithm based on an earlier work[47,54] was used to reconstruct the whole physical domain. A fifth-order blending function with $r(0) = 0$ and $r(1) = 1$ was used for dynamic mesh deformation. It is written as

$$r_5(s) = 10s^3 - 15s^4 + 6s^5, \quad s \in [0, 1], \tag{12}$$

where s represents the normalized distance between the present grid node and the moving boundaries. Changes in the position vector $\vec{P}$ for an arbitrary grid node can then be obtained as follows:

$$\Delta \vec{P}_{present} = (1 - r_5) \Delta \vec{P}_{rigid}. \tag{13}$$

When $r_5(0) = 0$, the grid node will move at the same speed with the moving boundary; and when $r_5(1) = 1$, the grid node will stay stationary.

D. Computational domain

The computational domain shown in Fig. 1 was used in the current study. The distance between the quarter chord location of the NACA0012 airfoil to the center of the gust is 1.08c, where c is the chord length of the airfoil. The gust width at the exit in this study is 1.06c. Note that the dimensions of the computational domain are calculated to match those from a wind tunnel experiment.[9] However, for

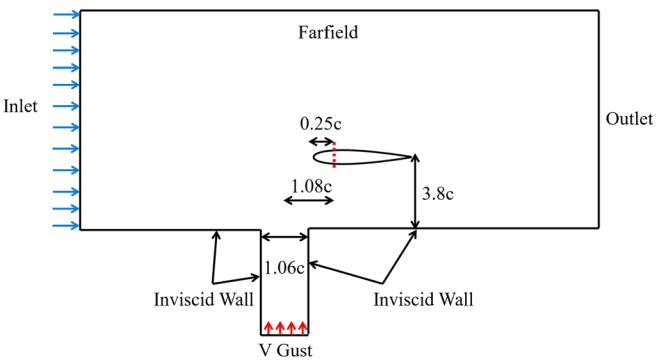

FIG. 1. An illustration of the computational domain.

this simulation a far field boundary was used for the top of the computational domain, which is different from the top wall of the wind tunnel. Results in previous studies[18] showed that this has a limited effect when compared to the wind tunnel tests. Fixed inlet and outlet boundaries, and an inviscid wall boundary on the bottom of the computational domain were enforced in the simulation. As observed in Fig. 1, a uniform incoming flow in the horizontal direction interacted with a jet of uniform vertical velocity generated ahead of and below the airfoil. Since non-dimensionalized Navier–Stokes equations were solved, the incoming flow velocity U_∞ was set as 1, and correspondingly, the Mach number was 0.1. The chord length of the airfoil was selected to generate a chord Reynolds number of Re = 12 000. The transient gust was generated by a cross-flow ducted floor jet and its interaction with the freestream flow caused the jet to bend downstream, thus creating a blockage effect and modifying the effective AoA over the airfoil in the freestream flow. For the gust inlet, a uniform vertical gust velocity of similar magnitude as the experimental setup[9] was given. The gust ratio (GR) is defined as the vertical speed V of gust divided by the freestream flow U_∞ (i.e., V/U_∞), which was 0.42 for all simulations presented in this paper.

III. VERIFICATION AND VALIDATION OF THE CFD SOLVER

As a first step, verification and validation (V&V) of the flow solver was conducted under uniform flow conditions, without the gust present. Numerical results were compared with published data from previous experiments and computations. Table I shows a comparison of the drag coefficient (C_D) at Reynolds number (Re) 12 000 at zero AoA under uniform flow conditions. The current drag coefficient agrees well with the reference data.[55–58]

For V&V of the flow solver when using moving grids, a common set of airfoil kinematics was implemented on the solver. In this study, a NACA0012 airfoil was pitched about its 1/4 chord with a sinusoidal motion, specifically expressed as follows:

$$\theta(t) = \theta_m + \theta_o \sin(2\pi f t + \phi), \tag{14}$$

where θ_m is the mean angle of attack, θ_o is the amplitude of the pitching angle, ϕ is the initial phase, f is the oscillating frequency, and t is the dimensional time. These types of problems are typically classified by using reduced frequency, k, and Strouhal number, S_t, which are defined as

$$k = \frac{\pi f c}{U_\infty}, \tag{15}$$

TABLE I. Comparison of C_D for NACA0012 at $Re = 12\,000$ and $AoA = 0^\circ$ in a uniform flow.

Sources	C_D
Current	0.0347
Hammer *et al.*[55]	0.0350
Laitone[56]	0.0334
Liu and Kawachi[57]	0.0346
Young and Lai[58]	0.0361

$$S_t = \frac{2 f A_{pitch}}{U_\infty}, \tag{16}$$

where c is the chord length of the airfoil, A_{pitch} is the pitching amplitude of the trailing edge of the airfoil, and U_∞ is the freestream velocity. The airfoil was oscillated at a variety of reduced frequencies for comparison with other work.[59] Figure 2 shows a comparison of average thrust coefficients for the pitching airfoil simulation with a pitching amplitude of 2° and 4° at Reynolds number 12 000. The results agree well with those in the prior study[59] for identical flow conditions. In general, a flow with an oscillating airfoil is dominated by the oscillating frequency and shed vortices. It has been shown that for a plunging airfoil, which represents a similar problem dominated by vortex structures, 2D and 3D results agree well when implicit large eddy simulation (i.e., no explicit turbulence modeling is used in simulations) is adopted.[60]

In our recent studies,[9,18] a comparison of gust–wing interaction between experimental results from a vertical gust generator in a wind tunnel and numerical results obtained with the high-order CFD tool, also used in this study, has been carried out. Reasonable agreement with experimental flow fields around a stationary airfoil interacting with a gust was achieved in those studies.

IV. RESULTS AND DISCUSSION

A. Gust–wing interaction over a stationary airfoil

To explore the effect of a vertical gust on the stationary airfoil, a simulation was first conducted with the airfoil placed at zero AoA (i.e., $\alpha = 0^\circ$) at a Reynolds number of Re = 12 000. To understand the effects of the gust, the forces acting on the airfoil were decomposed into horizontal (drag or thrust) and vertical (lift) directions with respect to the position of airfoil. The drag and lift coefficients are defined as

$$C_D = \frac{2F_X}{\rho U_\infty{}^2 A}, \tag{17}$$

$$C_L = \frac{2F_Y}{\rho U_\infty{}^2 A}, \tag{18}$$

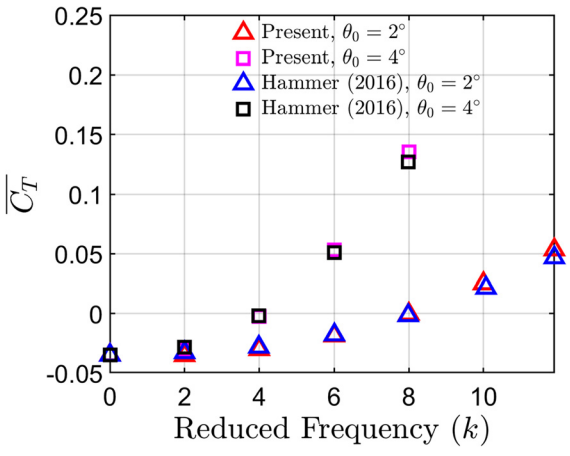

FIG. 2. Time-averaged thrust coefficients over a NACA0012 airfoil pitching about its quarter chord length at Re = 12 000 compared with the results from Hammer.[59]

where F_X is the drag force, F_Y is the lift force, ρ is the fluid density, U_∞ is the freestream velocity, and A is the area. Note that when C_D is negative, it indicates that a thrust is generated. For 2D problems, the force is measured per unit length; therefore, A is replaced with the chord length of the airfoil.

Figure 3 shows the lift and drag coefficient histories of the stationary NACA0012 airfoil with the gust developing in the vertical direction. Figure 3 clearly depicts the effect of the gust on lift and drag over time due to continuous changes in the effective AoA. Before $t^* = 20$, the gust was in an early development stage, and the airfoil experienced a sudden pressure wave propagation from the gust, resulting in several spikes in the lift coefficient history, such as a spike around the non-dimensionalized time $t^* = tU_\infty/c = 6$. After $t^* = 20$, the gust starts to interact with the airfoil more significantly. The results suggest that vertical gusts can cause a highly unsteady stall event on the airfoil. After around $t^* = 50$, the lift on the airfoil experienced fluctuations on the order of the peak steady lift. A lower gust ratio (GR = 0.21) was tested and showed similar results to the higher gust ratio case. For this lower gust ratio, the lift evolved more slowly and transitioned to unsteadiness later than the higher gust ratio shown in Fig. 3, but the same trend was observed.

Instantaneous vorticity fields around the airfoil at different times during the gust interaction are shown in Fig. 4. At early time ($t^* = 10$), the effect of the gust was minimal but after $t^* = 24$, the effects became more easily observed. At this time, the trailing edge separation became more pronounced with a notable vortex roll-up. When the gust continued to develop, a separation bubble on the suction side near the trailing edge grew, with some shear layer roll-up approaching the leading edge. After $t^* = 31$, these vortices formed on the upper surface and detached from the airfoil, forming vortex shedding as shown in Figs. 4(c) and 4(d). This effect occurred around the bend in lift observed around $t^* = 30$ in Fig. 3 and suggests the wing had entered a stalled state around this time. These shed vortices eventually formed near the leading edge and generated a transient low-pressure region on the upper surface of the airfoil, enhancing the lift. Once the gust was sufficiently developed, the airfoil experienced a highly unsteady leading edge vortex roll-up, somewhat similar to a dynamic stall event as shown in Figs. 4(e) and 4(f). It should be noted at this point the flow angle had changed so significantly that much of the lift generated was caused by the pressure side of the airfoil, with unsteady events dominating the stalled state.

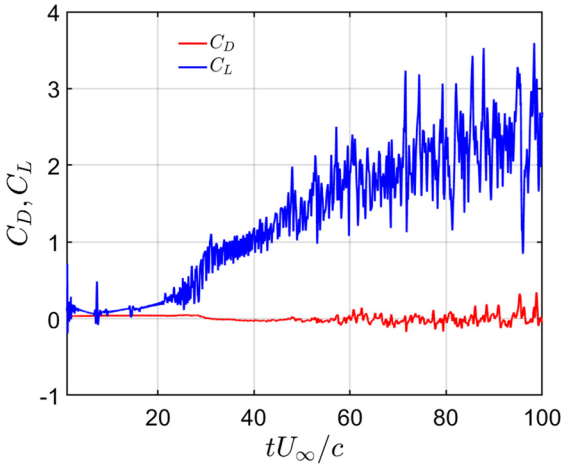

FIG. 3. Histories of drag and lift coefficients for NACA0012 at Re = 12 000 and AoA = 0° with gust developing in the vertical direction.

B. Gust–wing interaction with a pitch-down maneuver

The gust–stationary wing section showed a wing undergoing a highly unsteady stall event due to the change in effective AoA caused by the gust. Recent studies on gust mitigation[43,45,61] suggest that the gust effects can be controlled by changing the effective AoA induced by the gust. In this study, this control strategy was tested for a gust that developed over a longer time with a steady peak gust magnitude. The airfoil was pitched about the $c/4$ of the airfoil with a variety of response motions. These motions had a pre-set pitch-down magnitude to mimic a controller with a preprogramed gust response motion. The airfoil was pitched down to four different mean AoAs, namely, $\alpha_m = -12°, -18°, -22.8°$, and $-30°$, to change the effective AoAs induced by the gust after the non-dimensional time $t^* = 40$. These motions are shown in Eq. (19) and are based on pitching motions defined in Eldredge *et al.*[62] and Garmann *et al.*[63] Note that this geometric AoA variation approach was used to avoid discontinuities in the pitching rate.

$$\alpha(t) = \frac{\alpha_m}{2a\Delta T} ln\left(\frac{\cosh(a(T - T_1))}{\cosh(a(T - T_2))}\right) + \frac{1}{2}\alpha_m, \tag{19}$$

where a is the smoothness shape function parameter, which was 2.6 in the simulations; α_m is the maximum pitch-down angle, which was set to ramp from $\alpha_m = 0$ to $\tan^{-1}(V/U_\infty)$; T is the non-dimensional time ($T = tU_\infty/c$); and $\Delta T = T_2 - T_1$, where T_1 and T_2 are the non-dimensional time at which the motion to pitch-down maneuver would start and stop, respectively. The reduced pitch rate $K = \alpha_m c/(2U_\infty \Delta t)$ was varied to induce continuously changing AoAs. Note that an increase in a and decrease in ΔT can cause more abrupt motion.

The motion profiles of the AoA change are illustrated in Fig. 5(a). Figure 5(b) shows the corresponding lift coefficient histories for different pitch-down maneuver cases interacting with the growing vertical gust. When the pitch angle of the airfoil was larger than the effective AoA induced by the developing gust, the airfoil undergoes a negative lift overshoot with a large separation event on the lower surface of the airfoil; see Fig. 6. This overshoot stall was observed on all test cases except for the smallest motion. However, because the gust continued to grow during this time the lift coefficient rose to positive values over time. When the effective AoA of the gust grew after the pitch-down motion, the lift again started to fluctuate and the wing re-entered a stall state, see Fig. 5(b).

To avoid this overshoot stall while continuing to mitigate the gust effect, a stepwise pitch motion was tested. Figure 5(b) showed that the airfoil entered an unsteady stall state after non-dimensional time $t^* = 76$, following a pitch down of $\alpha_m = -12°$. Continuing this stepwise pitch-down behavior, the airfoil was further pitched down by $\alpha_m = -6°$, resulting in a geometric AoA of $\alpha_m = -18°$ and attached flow on the airfoil. As the gust-induced AoA continued growing, with a similar effect on lift, the lift again fluctuated around $t^* = 110$. At this point, the airfoil was again pitched down by $\alpha_m = -6°$. This process

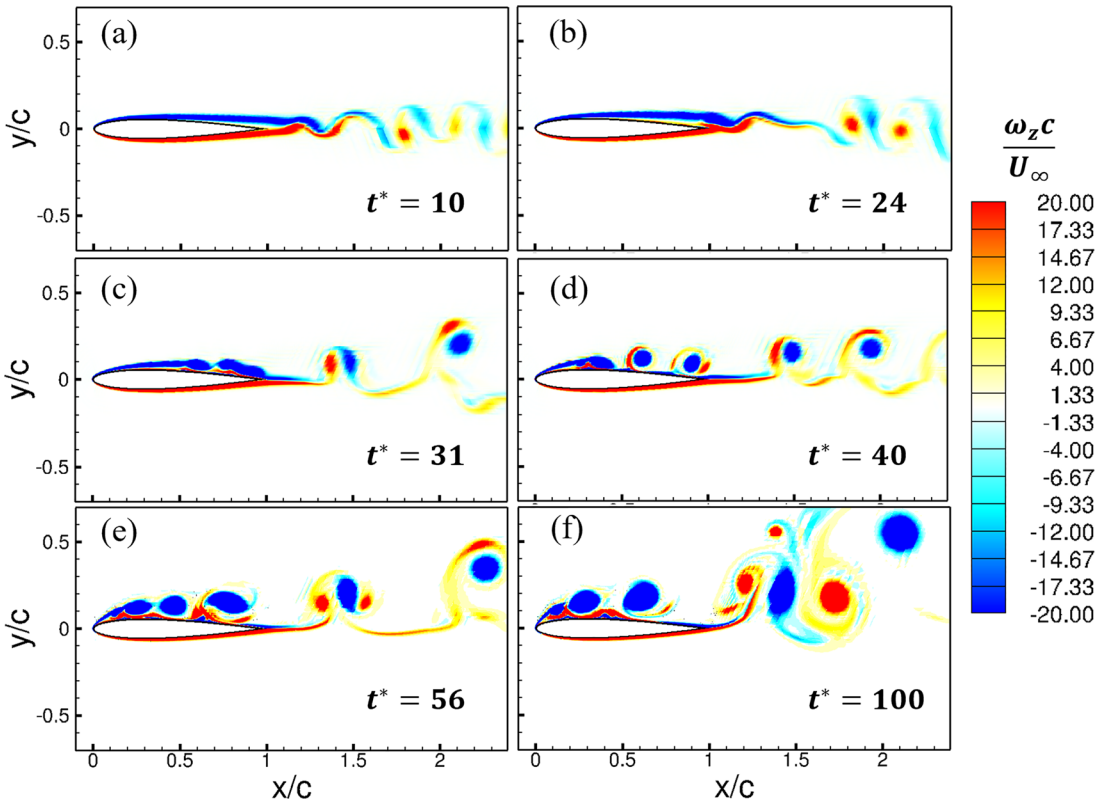

FIG. 4. Instantaneous vorticity fields around the airfoil at (a) $t^* = 10$, (b) $t^* = 24$, (c) $t^* = 31$, (d) $t^* = 40$, (e) $t^* = 56$, and (f) $t^* = 100$ at $Re = 12\,000$ during the gust development process.

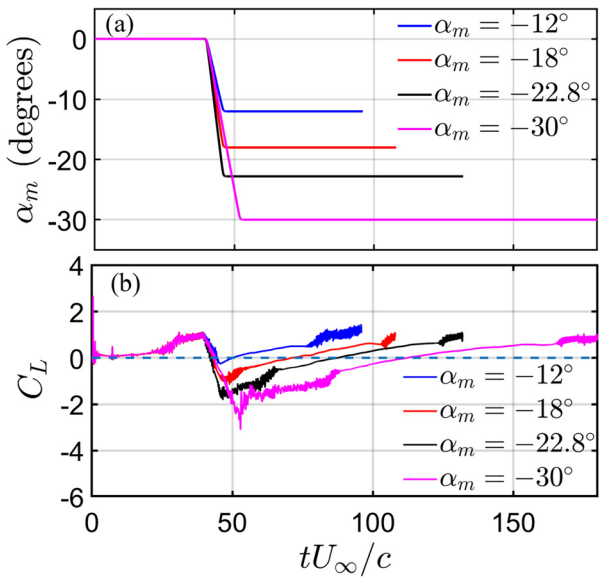

FIG. 5. (a) Pitch-down motion for different AoAs and (b) lift coefficient histories for the pitch-down airfoil at different effective AoAs.

was repeated until the geometric AoA of $\alpha_m = -30°$ was reached; see Fig. 7. Eventually, even at this significant downward pitch angle, the growing AoA caused by the gust exceeded the stall angle of the airfoil and unsteady lift was again observed. When a stepwise pitch-down motion was used, the lift overshooting phenomenon was suppressed and the lift fluctuation associated with traditional stall was also effectively suppressed. While a stepwise motion is somewhat atypical of

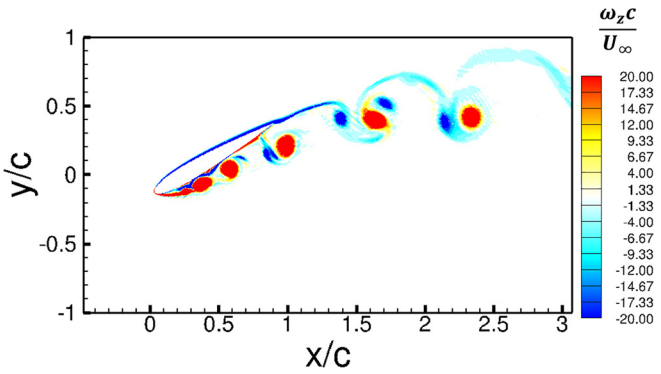

FIG. 6. Instantaneous vorticity field for the pitch-down airfoil with $\alpha_m = -30°$ at $t^* = 60$.

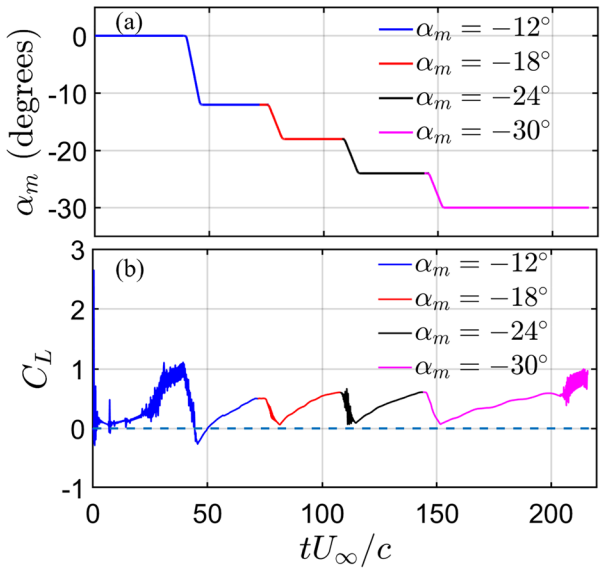

FIG. 7. (a) Stepwise pitch-down motion from $\alpha_m = 0°$ to $\alpha_m = -12°$, $\alpha_m = -18°$, $\alpha_m = -24°$, and $\alpha_m = -30°$ and (b) lift coefficient histories for the pitch-down airfoil with the stepwise pitch-down motion from $\alpha_m = 0°$ to $\alpha_m = -30°$.

aircraft motions, a stall sensor with a preprogramed pitch-down response is more likely to be implemented on MAV systems than a continuous closed-loop controller for gusts.

C. Gust–wing interaction over a pitching airfoil

1. Effect of reduced frequency

This section presents a novel method of vertical gust mitigation, which uses small amplitude airfoil oscillations to alter the flow and negate the effects of the gust. The effects of reduced frequency and Strouhal number are evaluated to determine the driving forces behind the interaction. A wide range of reduced frequencies were tested as documented in Table II. Note that the pitching amplitude for all these cases was fixed at $\theta_o = 10°$, which will result in different Strouhal numbers. The Reynolds number and the gust ratio (V/U_∞) remained at 12 000 and 0.42, respectively, to match the stationary wing case. The airfoil pitch frequencies considered in Table II were determined based on local peak frequencies observed in the power spectral density (PSD) of the lift data recorded during interaction between the vertical gust and the stationary airfoil, as shown in Fig. 8(a). Figure 8(b) shows

TABLE II. Pitching airfoil cases for varying reduced frequencies with a fixed pitching amplitude $\theta_o = 10°$.

Cases	Reduced frequencies	Strouhal numbers
1	0.79	0.065
2	1.16	0.096
3	2.86	0.237
4	3.64	0.302
5	4.46	0.370

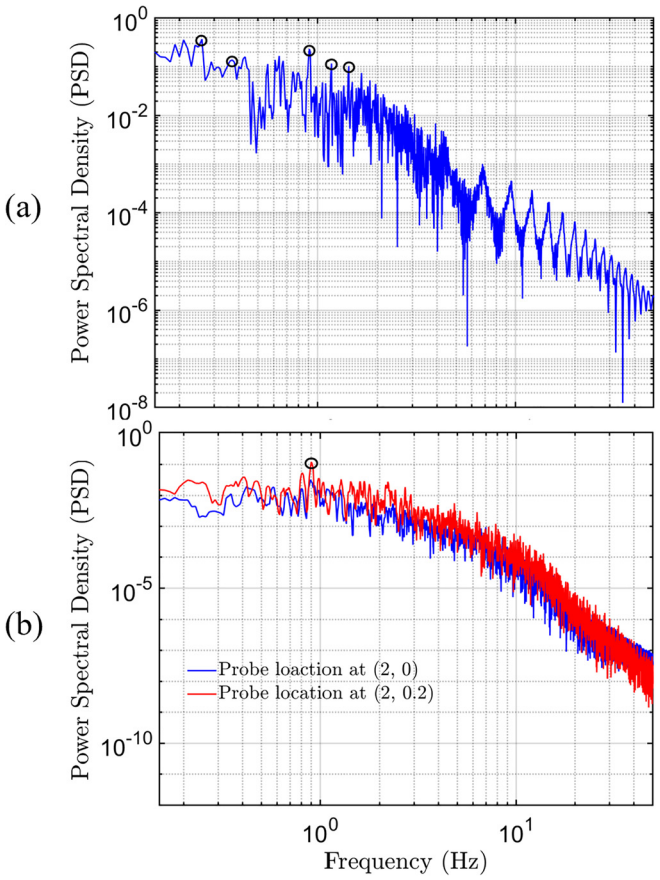

FIG. 8. PSD of (a) the lift coefficient and (b) the streamwise velocity probed at (x/c, y/c) = (2, 0) and (2, 0.2) in the wake region for NACA0012 at Re = 12 000 and AoA = 0° with gust.

the PSD of the streamwise velocity recorded in the wake region at two locations (x/c, y/c) = (2, 0) and (2, 0.2). Based on the PSD analysis of the velocity in the wake region, the vortex shedding frequency was observed around 0.91 Hz, which results in a reduced frequency of 2.86. This frequency appears as a local peak in both Figs. 8(a) and 8(b), and was selected as one of the oscillating frequencies for testing.

To simplify the analysis of the gust–wing interactions with the oscillating airfoil, the gust interaction was broken up into "early" and "later" stages. The early stage was defined as $t^* \leq 20$ and the later stage was defined as $t^* \in [30, 40]$. Force coefficients presented for early and later stages were averaged over these time frames. Figures 9 and 10 show the drag and lift coefficient histories of the pitching airfoil at the different reduced frequencies tested. The drag and lift coefficient histories of the stationary airfoil are also presented in the two figures for comparison purposes. At lower reduced frequencies, such as $k = 0.79$, the force histories have high-frequency fluctuations similar to the stationary airfoil. When the reduced frequency reached $k = 2.86$, the force histories became periodic and were dominated by the pitching frequency of the airfoil. In this case, the gust had a limited effect on the mean lift during the early stage. Later as the gust grows in magnitude, the mean lift rose accordingly in the same fashion as that

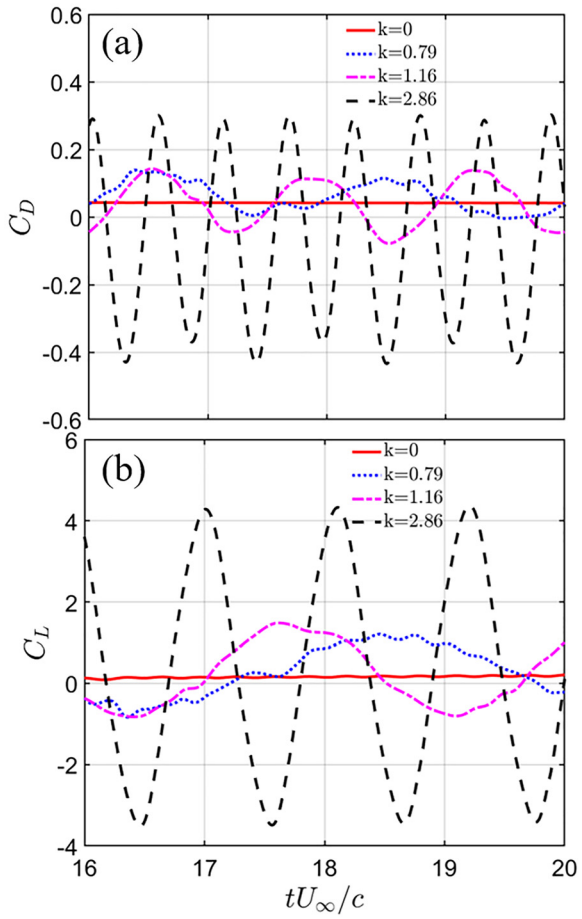

FIG. 9. (a) Drag and (b) lift coefficient histories for the pitching airfoil at different reduced frequencies, compared with those for the stationary airfoil during the early stage of gust development.

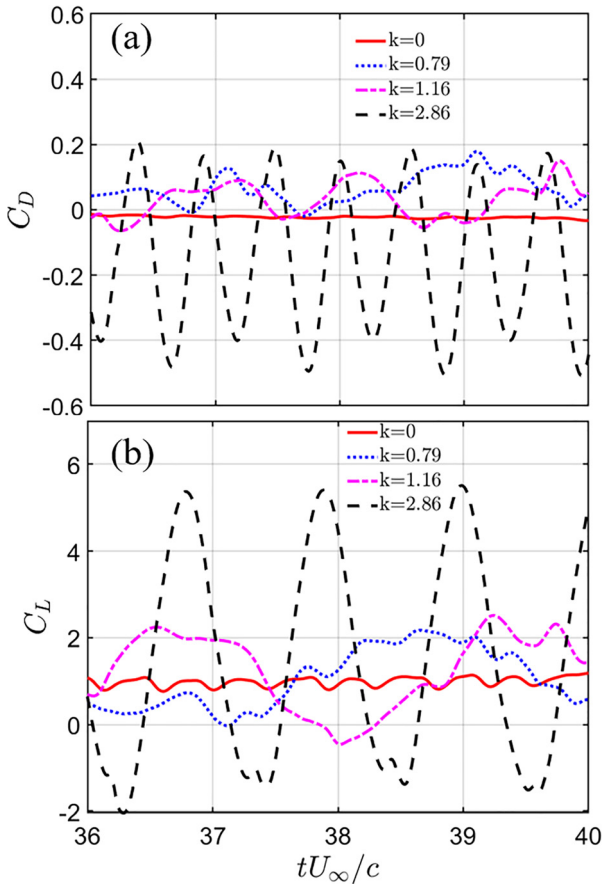

FIG. 10. (a) Drag and (b) lift coefficient histories for the pitching airfoil at different reduced frequencies, compared with those for the stationary airfoil during the later stage of gust development.

of the stationary airfoil; however, the force was still periodic with very small fluctuations. Similar phenomena were observed for the cases with higher reduced frequencies (not presented here). Higher reduced frequency cases appeared to completely mitigate the unsteadiness caused by the gust.

Figure 11 shows the time averages of the aerodynamic force coefficients of the airfoil for the stationary airfoil and the oscillating airfoils at different reduced frequencies during the early gust development stage (i.e., $t^* \leq 20$) and a later gust–wing interaction stage (i.e., $t^* \in [20, 40]$). The average for the early gust–wing interaction stage is carried out from $t^* = 10$ to 20, during which the gust had limited influence on the airfoil. At the later stage, the average was calculated from $t^* = 30$ to 40. Note that for pitching airfoil cases, the average was calculated with the maximum number of pitching cycles that can be fit into the ten non-dimensional time periods to eliminate any pitching cycle-related bias. Figure 11(a) shows that drag was gradually converted to thrust as the reduced frequency increased, which was expected for an oscillating airfoil. At the later stage, the interaction between the gust and the airfoil further increased this thrust production. At the early gust–wing interaction stage, the gust slightly increased the average lift coefficients ($\overline{C_L}$) when compared to the static airfoil. $\overline{C_L}$ for the cases with higher reduced frequencies was significantly increased due to the intense gust–wing interaction at the later stage. The case with $k = 2.86$ produced the maximum $\overline{C_L}$, see Fig. 11(b).

Two statistics were used to quantitatively evaluate the effectiveness of gust mitigation: power consumption and the smoothness of the lift coefficient history. An effective pitching strategy would exhibit a desired level of smoothness, which reflects lift predictability, with minimum power consumption. The power $P(t)$ required to pitch the airfoil is calculated with the following formula:

$$P(t) = -M(t)\frac{d\theta}{dt}, \tag{20}$$

where $M(t)$ is the pitching moment about the quarter chord length of the airfoil and $d\theta/dt$ is the angular velocity. Note that $M(t)$ can be estimated from the aerodynamic pitching moment as long as the inertia of the airfoil is very small. The dimensionless power coefficient is expressed as

$$C_p = \frac{P(t)}{0.5\rho c {U_\infty}^3} = -C_M(t)\frac{d\theta}{dt^*}, \tag{21}$$

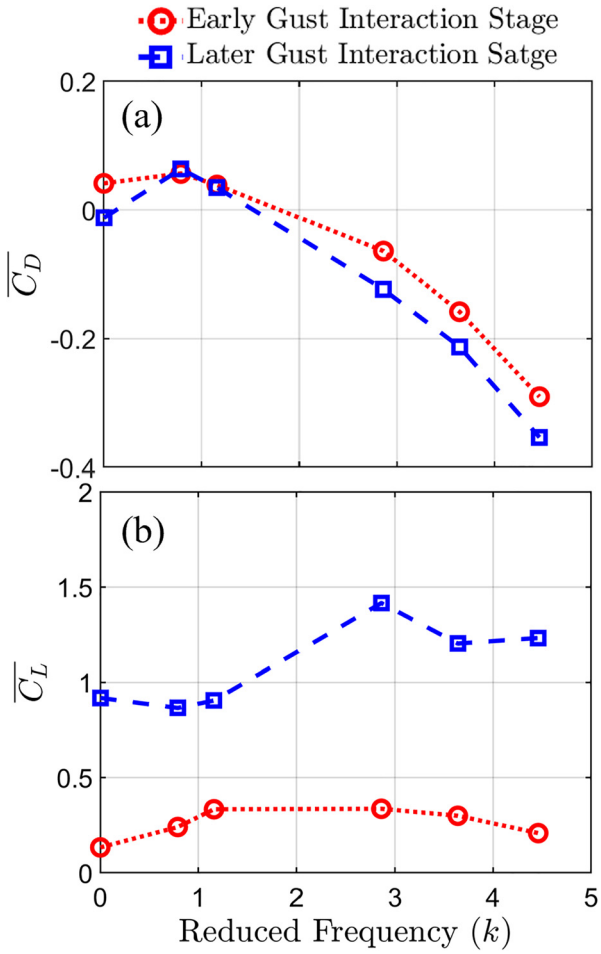

FIG. 11. Time-averaged aerodynamic forces before and after intensive gust–wing interaction. (a) Drag coefficient and (b) lift coefficient for the stationary and pitching airfoils at different reduced frequencies.

where C_p and C_M are the power and moment coefficients, respectively. Figure 12 shows the average power coefficients of the pitching airfoil at different reduced frequencies for early and late gust interaction. As expected, the power coefficient of the oscillating airfoil increased with increasing reduced frequency. Interestingly, the interaction with the gust lowered the power coefficient with a maximum benefit at $k = 2.86$, the same location where mean lift peaked.

The smoothness of the lift coefficient history was measured with a new parameter named "relative fluctuation." It is defined as the ratio between the L_2 norm (i.e., the square root of the "energy") of the fluctuation of any curve and that of the curve itself. The fluctuation was obtained by subtracting the smoothed curve after filtering from the original curve. In this test, a Gaussian filter with a filtering window size of 1/6 pitching cycle was used to generate the smoothed curve. Two examples at $k = 0.79$ and 4.46 are used to explain this idea. As shown in Fig. 13, there are many small-scale fluctuations in the lift coefficient history when $k = 0.79$ and these fluctuations have been smoothed out after filtering. Since this case had significant deviations from the smoothed curve, a large relative fluctuation of 0.0836 was

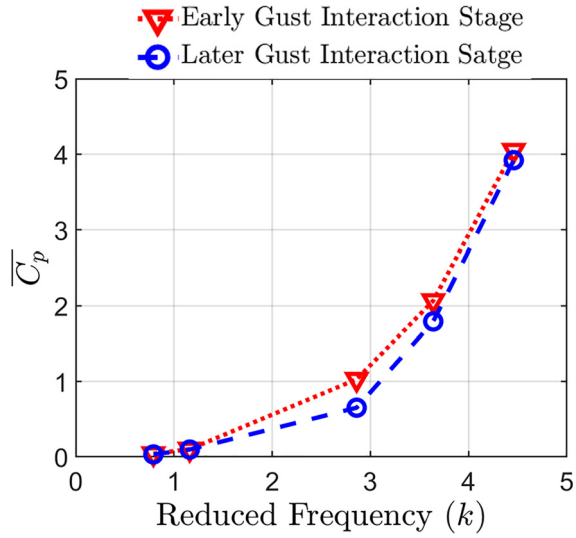

FIG. 12. Time-averaged power coefficients of pitching airfoils at different reduced frequencies.

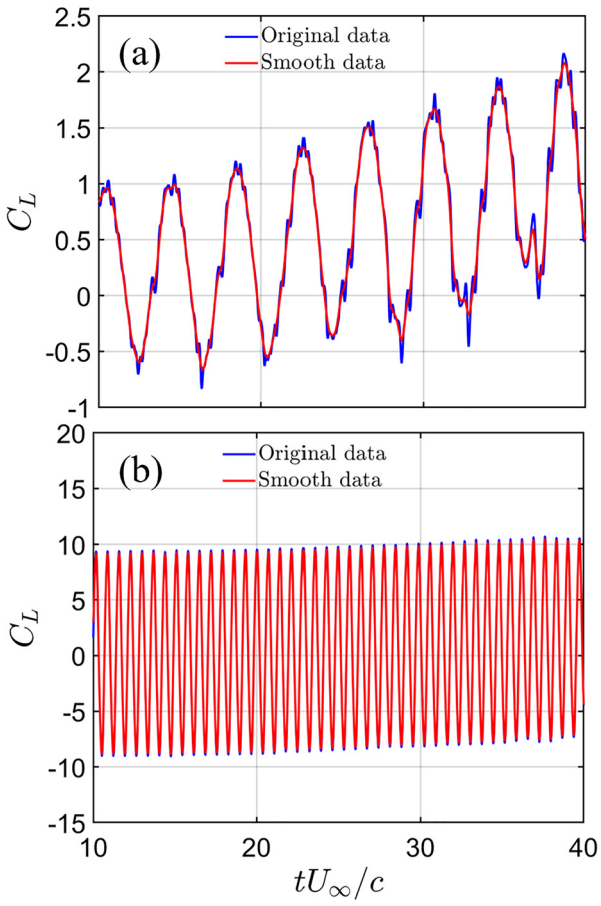

FIG. 13. Smoothed C_L compared to the original C_L of pitching airfoils at (a) $k = 0.79$ and (b) $k = 4.46$.

TABLE III. Relative fluctuation for pitching airfoil cases at varying reduced frequencies with fixed pitching amplitude $\theta_o = 10^\circ$.

Cases	Reduced frequencies	Relative fluctuation
1	0.79	8.36×10^{-2}
2	1.16	4.53×10^{-2}
3	2.86	2.16×10^{-2}
4	3.64	2.11×10^{-2}
5	4.46	2.12×10^{-2}

observed (see Table III). When $k = 4.46$, only the peak values are smoothed out, which generated a small relative fluctuation about 0.0212. By calculating the relative fluctuations of sinusoidal curves with angular frequencies ranging from 1 to 100 (note that the angular frequency of the $k = 0.79$ case is 1.58 rad/s in this study), the mean value of relative fluctuation was observed to be around 0.02 when the Gaussian filter with a filtering window size of 1/6 oscillation cycle was used. This indicates that when the relative fluctuation is close to 0.02, the curve is similar to a sinusoidal one, which is infinitely smooth.

The relative fluctuations of the lift coefficients for all cases with different reduced frequencies are summarized in Table III. At lower reduced frequencies, the relative fluctuation was larger when compared to those at higher reduced frequencies, suggesting less effective mitigation of the gust at low reduced frequencies. The relative fluctuations for cases with higher reduced frequency ($k \geq 2.86$) are very similar to each other. Based on the cases tested in the current study, a reduced frequency of $k = 2.86$ was found to be the optimal reduced frequency for gust mitigation. The corresponding oscillating frequency for the optimal reduced frequency ($k = 2.86$) was the same as the dominant vortex shedding frequency found from the PSD analysis of the velocity in the wake region of the stationary airfoil interacting with the gust as shown in Fig. 8(b). An increase in reduced frequency beyond this point did not have a significant impact on vertical gust mitigation. As reported by Fisher *et al.*,[21] compared to a stationary wing, the flapping wing is less sensitive to turbulent environment and the flapping motion dominates the creation of major flow features when the reduced frequency is increased. In this study, the same phenomenon has been observed in the context of gust–pitching airfoil interaction.

Analysis of the flow fields was done to correlate flow structures with the effects of reduced frequencies discussed above. Figure 14 depicts the instantaneous vorticity fields around pitching airfoils with three (i.e., low, medium, and high) reduced frequencies during the early (left column of Fig. 14) and later (right column) stages of gust–wing interaction. At the early stage of gust development, the vortex

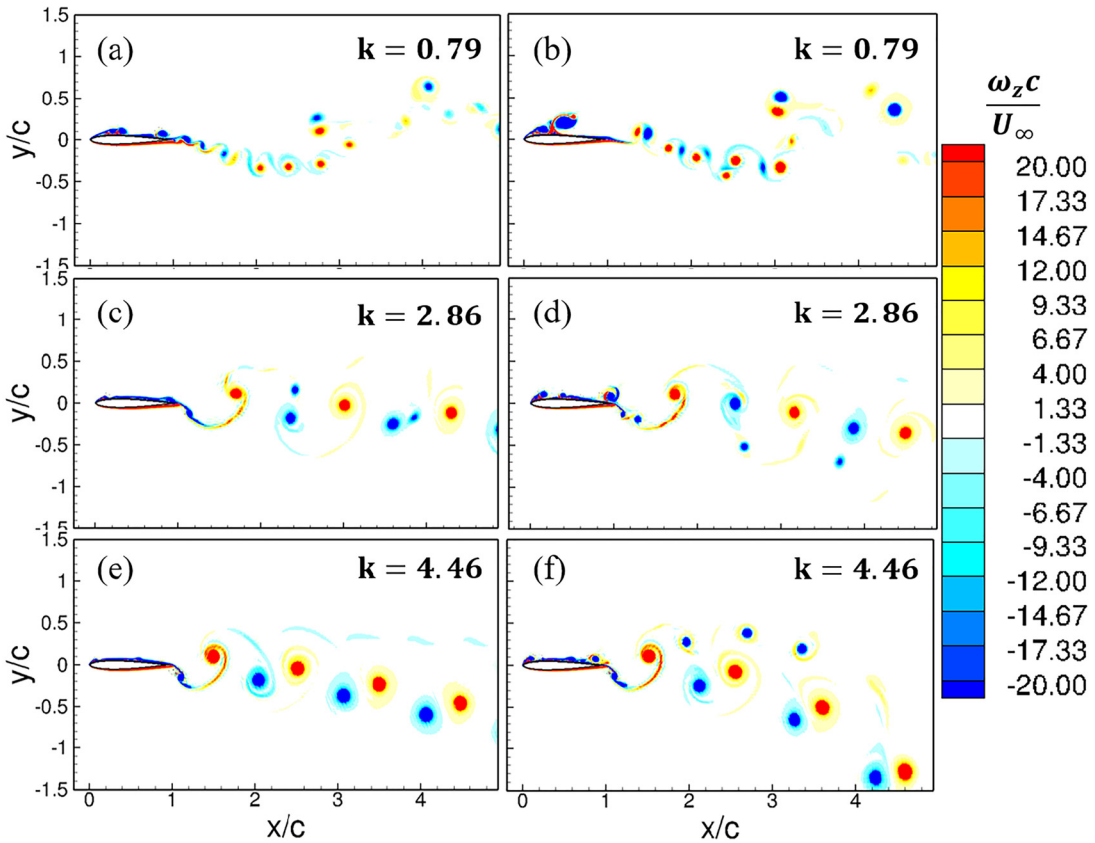

FIG. 14. Instantaneous vorticity fields of pitching airfoils at different reduced frequencies during the early (left) and later (right) gust–wing interaction stages. [(a) and (b)] The reduced frequency $k = 0.79$; [(c) and (d)] the reduced frequency $k = 2.86$; and [(e) and (f)] the reduced frequency $k = 4.46$.

shedding pattern from the airfoil was similar to that of an airfoil pitching at the same reduced frequency under a uniform flow condition. Smaller shed vortices were formed on the upper side of the rapidly pitching airfoil compared to the cases with lower reduced frequencies. At high reduced frequencies, such as $k = 2.86$ and 4.46, a reverse von Karman vortex street was formed, reflective of the thrust generation behavior observed in the data. In general, wake structures were unaffected by the gust during the early gust development stage.

Compared to the early gust–wing interaction stage, during the later interaction stage larger vortices appeared on top of the pitching airfoil, especially for the low reduced frequency case ($k = 0.79$), see Fig. 14(b). When the airfoil was pitched at a reduced frequency higher than $k = 2.86$, as shown in Figs. 14(d) and 14(f), the vortices near the top surface were much smaller than those at lower reduced frequencies at the same stage of gust development. These vortices also evolved more slowly and remain closer to the airfoil at higher reduced frequencies when compared with the lower reduced frequency cases. This suggests that at higher pitching frequencies, the flow features were dominated by the pitch motion, which in turn substantially suppressed the effects of the gust. The effect of reduced frequency was similar when tested for a lower gust ratio case (GR = 0.21). Unlike the pitch-down control strategy presented in Sec. IV B, the gust–wing interaction was always dominated by the pitch motion when the reduced frequency was sufficiently high. As a result, the highly unsteady lift fluctuation induced by the gust can always be fully mitigated by the pitching airfoil during long-duration gust–wing interaction. When the gust was fully developed, the only impact of the gust on the pitching airfoil was to increase its average lift coefficient, as demonstrated in Fig. 11. Based on this result, it is apparent that an oscillating airfoil motion could be used to mitigate a gust during gust development, with potential to return to steady attached flow once the unsteady gust has stabilized.

2. Effect of pitching amplitude

The results in Sec. C 1 demonstrated that increasing reduced frequency with a constant pitching amplitude of $\theta_o = 10^\circ$ can mitigate the vertical gust effects. A reduced frequency of $k = 2.86$ was the most effective one tested in mitigating the gust effects. This section aims to gain insight into the effects of pitching amplitudes (i.e., Strouhal numbers when the reduced frequency is fixed) on gust mitigation by varying the pitch amplitude at the optimal reduced frequency $k = 2.86$. The cases tested are summarized in Table IV.

Figures 15 and 16 show the instantaneous forces histories for pitching airfoils with different pitching amplitudes at the optimal reduced frequency $k = 2.86$ during the early and later gust–wing interaction stages, respectively. Although the vertical gust during the later gust–wing interaction stage was much stronger compared to that during the early stage, the force variation patterns for all cases were very similar during the two stages. The drag coefficient was slightly shifted toward the negative, thus enhancing thrust generation, and the lift coefficient was shifted to a more positive value, increasing the time-averaged lift. These results suggest that the pitching amplitude (correspondingly, the Strouhal number) is not a dominant factor for gust mitigation; instead, the reduced frequency is the dominant one.

TABLE IV. Pitching airfoil cases at optimal reduced frequency with varying pitching amplitude.

Cases	Pitching amplitude (θ_o)	Strouhal numbers
1	2°	0.06
2	4°	0.12
3	8°	0.24
4	16°	0.48

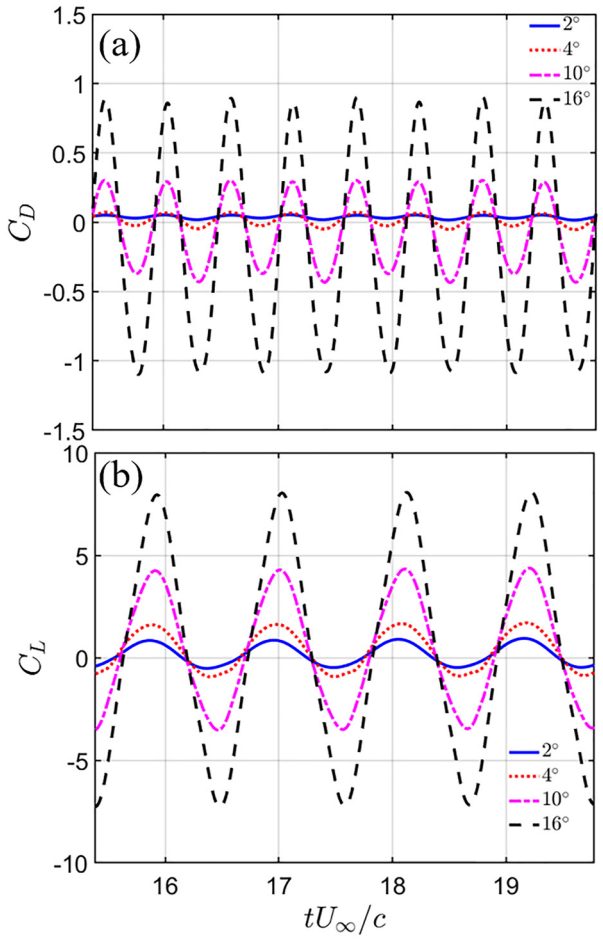

FIG. 15. (a) Drag and (b) lift coefficient histories for the pitching airfoil with different pitching amplitudes during the early stage of gust development at $k = 2.86$.

Figures 17 and 18 present the time-averaged aerodynamic forces and power consumption of the pitching airfoil with different pitching amplitudes at the optimal reduced frequency $k = 2.86$ during the early and later gust–wing interaction stages. For lower pitching amplitudes (i.e., $\theta_0 = 2^\circ$ and 4°), drag was produced during the early gust–wing interaction stage while thrust is produced in the later gust–wing interaction stage; see Fig. 17(a). For larger pitching amplitudes, thrust was always produced during both the early and later gust–wing interaction stages; see Fig. 17(b). The time-averaged thrust increased with the pitching amplitude. The time-averaged lift coefficients seem not to be significantly affected by the pitching amplitude during the early gust–wing interaction stage. However, high pitching amplitudes can

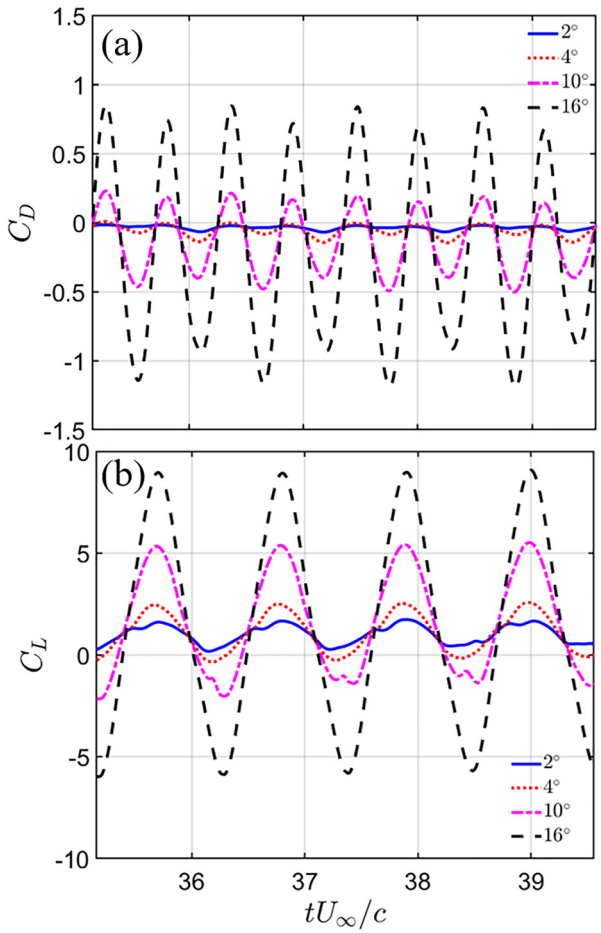

FIG. 16. (a) Drag and (b) lift coefficient histories for the pitching airfoil with different pitching amplitudes during the later stage of gust development at $k = 2.86$.

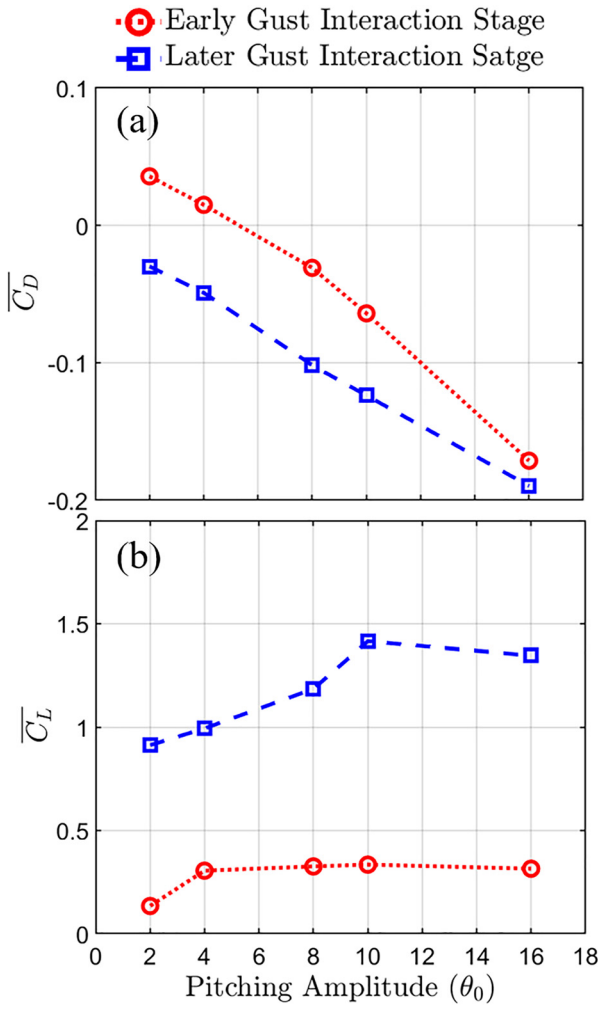

FIG. 17. Time-averaged aerodynamic forces before and after intensive gust–wing interaction. (a) Drag coefficient and (b) lift coefficient for the stationary and pitching airfoils with different pitching amplitudes at $k = 2.86$.

increase the time-averaged lift coefficients during the later gust–wing interaction stage, and lift is maximized when the pitching magnitude is 10°. As expected, the power consumption increased when the pitching amplitude increased, as shown in Fig. 18. One interesting observation is that the power consumption of the pitching airfoil during the later gust–wing interaction stage was smaller than that during the early stage, especially when the pitching amplitude was large.

To measure the gust mitigation effectiveness, the relative fluctuation approach used in Sec. IV C 1 is used for varied pitching amplitudes. Table V documents the relative fluctuations for the pitching airfoils with different pitching amplitudes at the optimal reduced frequency $k = 2.86$. These results showed that the relative fluctuations for different pitching amplitudes all have similar values. It is clear that the effects of the gust can be mitigated even with the lowest pitching amplitude at the optimal reduced frequency. This again confirms that the reduced frequency is the dominant factor for mitigating the effects of vertical gusts.

The flow fields around the pitching airfoil with different pitching amplitudes at the optimal reduced frequency $k = 2.86$ are shown in Fig. 19, which depicts the instantaneous vorticity fields during the early (left column) and later (right column) gust–wing interaction stages. During the early gust–wing interaction stage, vortices were not formed near the leading edge for lower pitching amplitudes (i.e., $\theta_0 = 2°$ and 4°); see Figs. 19(a) and 19(c). However, for the case with $\theta_0 = 16°$, these vortices were formed. During the later gust–wing interaction stage, leading-edge vortices were present in all cases. The size of these vortices was smaller when the airfoil was pitched with lower pitching amplitude due to the smaller AoA of the pitching motion. In addition, Figs. 19(e) and 19(f) reveal that the airfoil pitching at larger pitching amplitudes results in stronger and more organized reverse von Karman vortex street in the wake region, which results in the significant increase in thrust production observed earlier.

V. CONCLUSION

This work presented a numerical investigation of gust–wing interactions at low Reynolds numbers with advanced high-order CFD methods and identified key dynamics that provide clues to multiple gust mitigation strategies. For a stationary airfoil, the gust caused an

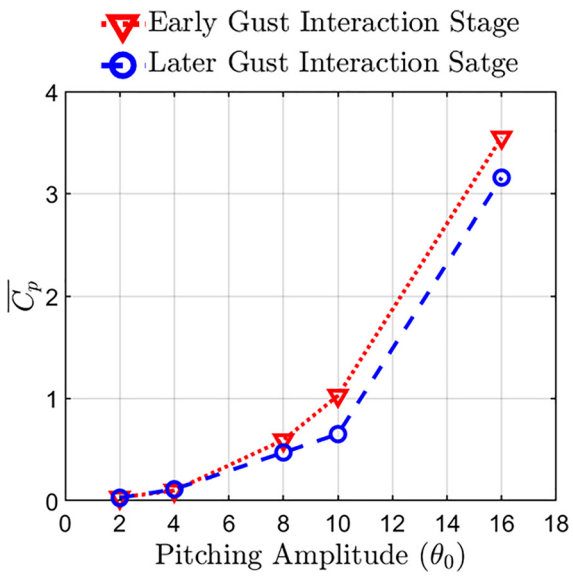

FIG. 18. Time-averaged power coefficients of pitching airfoils with different pitching amplitudes at $k = 2.86$.

TABLE V. Relative fluctuation for pitching airfoil cases with varying pitching amplitudes θ_o at the optimal reduced frequency $k = 2.86$.

Cases	Pitch amplitude	Relative fluctuation
1	2°	1.89×10^{-2}
2	4°	1.99×10^{-2}
3	8°	2.12×10^{-2}
4	10°	2.16×10^{-2}
5	16°	2.28×10^{-2}

increase in lift followed by a highly unsteady stall process. A pitch-down maneuver was demonstrated as an effective method of responding to the gust, and it was further observed that the effects of the gusts can be mitigated with a simple pitch response maneuver. A larger change in pitch angle was observed to cause negative lift with a high potential to overshoot into a negative angle stall state. A stepwise pitch-down approach was demonstrated as an effective method for maintaining steady lift even when the AoA generated by the gust continued to grow. These results also suggest that a stepwise response leveraging a stall sensor might be a lower cost mechanism for gust response compared to a more complicated closed-loop controller.

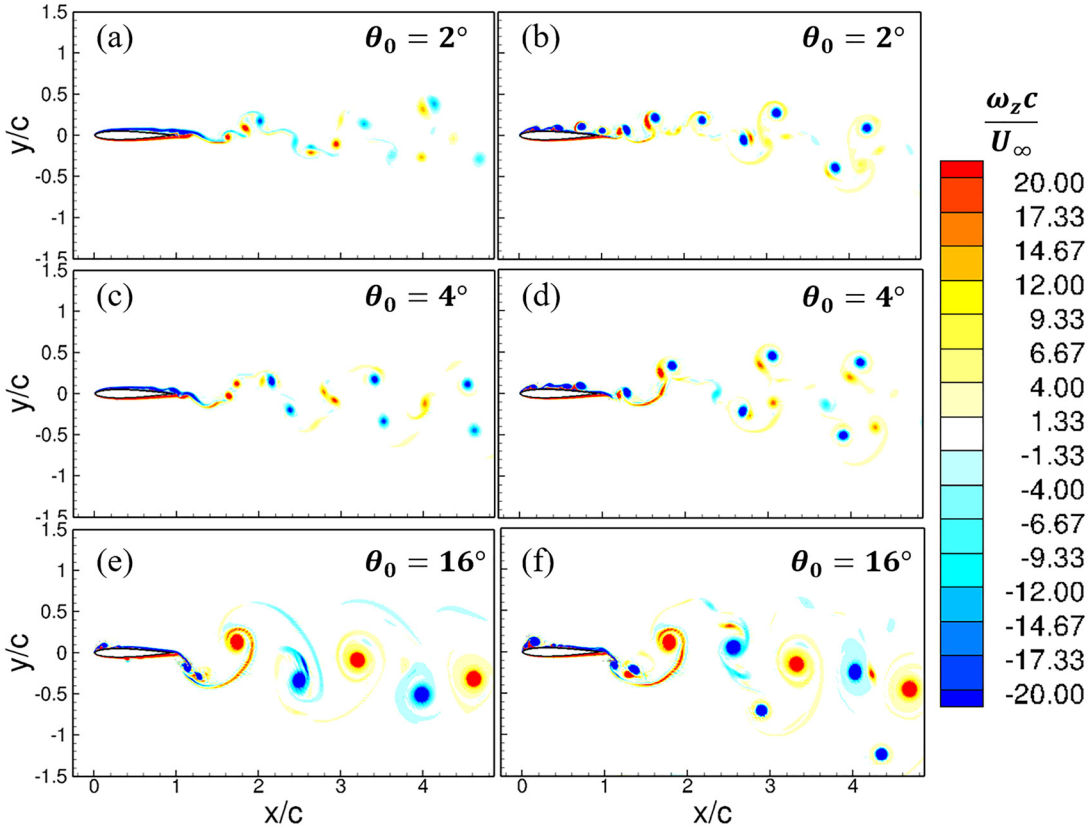

FIG. 19. Instantaneous vorticity fields of pitching airfoils at different pitching amplitude at $k = 2.86$ during the early (left) and later (right) gust interaction stages. [(a) and (b)] The pitching amplitude $\theta_0 = 2°$; [(c) and (d)] the pitching amplitude $\theta_0 = 4°$; and [(e) and (f)] the pitching amplitude $\theta_0 = 16°$.

A gust mitigation strategy using oscillating airfoils was also demonstrated. The influence of reduced frequency and Strouhal number was evaluated and it was shown that oscillating the airfoil had several different effects. At low reduced frequencies, the gust continues to dominate the flow field and force coefficients, generating highly unsteady noise on top of the typically sinusoidal lift curves generated by pitching airfoils. Pitching at higher reduced frequencies overcomes the flow disturbances caused by the vertical gust. However, the gust significantly increased both the lift and thrust generated by the oscillatory motion, with the average lift shifting above the static stall lift. A relative fluctuation metric along with power consumption was used to evaluate the effectiveness of the gust mitigation strategy. The optimal reduced frequency using these metrics was $k = 2.86$, which had a low relative fluctuation with the lowest power consumption. Results also showed that the Strouhal number was not a dominant factor when attempting to mitigate a vertical gust. At the optimal reduced frequency the Strouhal number, as varied by controlling oscillating amplitude, had little effect on the relative fluctuation, suggesting that even small amplitude oscillations can be used to mitigate gusts.

The current work demonstrates mitigation of gusts by generating large-scale unsteady features around the airfoil. However, the underlying flow physics generating these structures, such as that from the nonlinear vortex interaction at different spatiotemporal scales, is beyond the scope of this study and is left for discussion in future work on this topic.

ACKNOWLEDGMENTS

This research was sponsored by the Army Research Laboratory and was accomplished under Cooperative Agreement No. W911NF-20–2-0028. The views and conclusions contained in this document are those of the authors and should not be interpreted as representing the official policies, either expressed or implied, of the Army Research Laboratory or the U.S. Government. The U.S. Government is authorized to reproduce and distribute reprints for Government purposes notwithstanding any copyright notation herein. The hardware used in the computational studies is part of the UMBC High Performance Computing Facility (HPCF). The facility is supported by the U.S. National Science Foundation through the MRI program (Grant Nos. CNS-0821258, CNS-1228778, and OAC-1726023) and the SCREMS program (Grant No. DMS-0821311), with additional substantial support from the University of Maryland, Baltimore County (UMBC).

DATA AVAILABILITY

The data that support the findings of this study are available from the corresponding author upon reasonable request.

REFERENCES

[1]W. Shyy, H. Aono, S. K. Chimakurthi, P. Trizila, C.-K. Kang, C. E. Cesnik, and H. Liu, "Recent progress in flapping wing aerodynamics and aeroelasticity," Prog. Aerosp. Sci. **46**, 284–327 (2010).
[2]M. F. Platzer, K. D. Jones, J. Young, and J. C. Lai, "Flapping wing aerodynamics: Progress and challenges," AIAA J. **46**, 2136–2149 (2008).
[3]D. G. Bohl and M. M. Koochesfahani, "MTV measurements of the vortical field in the wake of an airfoil oscillating at high reduced frequency," J. Fluid Mech. **620**, 63–88 (2009).
[4]M. R. Visbal, R. E. Gordnier, and M. C. Galbraith, "High-fidelity simulations of moving and flexible airfoils at low Reynolds numbers," in *Animal Locomotion* (Springer, 2010), pp. 341–360.
[5]M. Ashraf, J. Young, and J. Lai, "Reynolds number, thickness and camber effects on flapping airfoil propulsion," J. Fluids Struct. **27**, 145–160 (2011).
[6]A. Mackowski and C. Williamson, "Direct measurement of thrust and efficiency of an airfoil undergoing pure pitching," J. Fluid Mech. **765**, 524–543 (2015).
[7]H. G. Küssner, "Zusammenfassender bericht über den instationären auftrieb von flügeln," Luftfahrtforschung **13**, 410–424 (1936).
[8]T. H. von Karman and W. R. Sears, "Airfoil theory for non-uniform motion," J. Aeronaut. Sci. **5**, 379–390 (1938).
[9]Z. F. Smith, A. R. Jones, and J. T. Hrynuk, "Micro air vehicle scale gust-wing interaction in a wind tunnel," AIAA Paper No. 2018-0573, 2018.
[10]J. An, Z. Yan, C. Qiu, and W. Zhou, "The numerical computation of aircraft response to arbitrary vertical gust distributions," J. Aircraft **22**, 988–992 (1985).
[11]Y. Lian and W. Shyy, "Aerodynamics of low Reynolds number plunging airfoil under gusty environment," AIAA Paper No. 2007-71, 2007.
[12]Y. Lian, "Numerical study of a flapping airfoil in gusty environments," AIAA Paper No. 2009-3952, 2009.
[13]X. Xu, X. Zhu, Z. Zhou, and M. Chang, "Numerical simulation of gust response for UAV airfoil," in *Proceedings of the 2010 Asia-Pacific International Symposium on Aerospace Technology* (Northwestern Polytechnical University, 2010), Vol. 1, p. 403.
[14]C. Liauzun, "Aeroelastic response to gust using CFD techniques," in *Proceedings of the ASME 2010 3rd Joint US-European Fluids Engineering Summer Meeting collocated with 8th International Conference on Nanochannels, Microchannels, and Minichannels* (ASME, 2011), 269–276.
[15]M. Jones and N. Yamaleev, "The effect of a gust on the flapping wing performance," AIAA Paper No. 2012-1080, 2012.
[16]G. Perrotta and A. R. Jones, "Unsteady forcing on a flat-plate wing in large transverse gusts," Exp. Fluids **58**, 101 (2017).
[17]S. Corkery, H. Babinsky, and J. Harvey, "On the development and early observations from a towing tank-based transverse wing–gust encounter test rig," Exp. Fluids **59**, 135 (2018).
[18]N. Poudel, M. Yu, Z. F. Smith, and J. T. Hrynuk, "A combined experimental and computational study of a vertical gust generator in a wind tunnel," AIAA Paper No. 2019-2166, 2019.
[19]H. Biler, G. Sedky, A. R. Jones, M. Saritas, and O. Cetiner, "Experimental investigation of transverse and vortex gust encounters at low Reynolds numbers," AIAA J. **59**, 786–799 (2021).
[20]I. Andreu-Angulo, H. Babinsky, H. Biler, G. Sedky, and A. R. Jones, "Effect of transverse gust velocity profiles," AIAA J. **58**, 5123–5133 (2020).
[21]A. Fisher, S. Ravi, S. Watkins, J. Watmuff, C. Wang, H. Liu, and P. Petersen, "The gust-mitigating potential of flapping wings," Bioinspiration Biomimetics **11**, 046010 (2016).
[22]J. Vance, I. Faruque, and J. Humbert, "Kinematic strategies for mitigating gust perturbations in insects," Bioinspiration Biomimetics **8**, 016004 (2013).
[23]S. Ravi, J. D. Crall, L. McNeilly, S. F. Gagliardi, A. A. Biewener, and S. A. Combes, "Hummingbird flight stability and control in freestream turbulent winds," J. Exp. Biol. **218**, 1444–1452 (2015).
[24]S. Ravi, D. Kolomenskiy, T. Engels, K. Schneider, C. Wang, J. Sesterhenn, and H. Liu, "Bumblebees minimize control challenges by combining active and passive modes in unsteady winds," Sci. Rep. **6**, 35043 (2016).
[25]P. Chirarattananon, Y. Chen, E. F. Helbling, K. Y. Ma, R. Cheng, and R. J. Wood, "Dynamics and flight control of a flapping-wing robotic insect in the presence of wind gusts," Interface Focus **7**, 20160080 (2017).
[26]M. Gu, J. Wu, and Y. Zhang, "Wing rapid responses and aerodynamics of fruit flies during headwind gust perturbations," Bioinspiration Biomimetics **15**, 056001 (2020).
[27]H. Liu, D. Kolomenskiy, T. Nakata, and G. Li, "Unsteady bio-fluid dynamics in flying and swimming," Acta Mech. Sin. **33**, 663–684 (2017).
[28]V. M. Ortega-Jimenez, J. S. Greeter, R. Mittal, and T. L. Hedrick, "Hawkmoth flight stability in turbulent vortex streets," J. Exp. Biol. **216**, 4567–4579 (2013).
[29]V. M. Ortega-Jimenez, N. Sapir, M. Wolf, E. A. Variano, and R. Dudley, "Into turbulent air: Size-dependent effects of von Kármán vortex streets on

hummingbird flight kinematics and energetics," Proc. R. Soc. B **281**, 20140180 (2014).
[30]V. M. Ortega-Jimenez, M. Badger, H. Wang, and R. Dudley, "Into rude air: Hummingbird flight performance in variable aerial environments," Philos. Trans. R. Soc. B **371**, 20150387 (2016).
[31]T. Engels, D. Kolomenskiy, K. Schneider, F.-O. Lehmann, and J. Sesterhenn, "Bumblebee flight in heavy turbulence," Phys. Rev. Lett. **116**, 028103 (2016).
[32]J. Crall, J. Chang, R. Oppenheimer, and S. Combes, "Foraging in an unsteady world: Bumblebee flight performance in field-realistic turbulence," Interface Focus **7**, 20160086 (2017).
[33]J. A. Cheney, J. P. Stevenson, N. E. Durston, J. Song, J. R. Usherwood, R. J. Bomphrey, and S. P. Windsor, "Bird wings act as a suspension system that rejects gusts," Proc. R. Soc. B **287**, 20201748 (2020).
[34]T. Nakata, R. Noda, S. Kumagai, and H. Liu, "A simulation-based study on longitudinal gust response of flexible flapping wings," Acta Mech. Sin. **34**, 1048–1060 (2018).
[35]M. A. Badger, H. Wang, and R. Dudley, "Avoiding topsy-turvy: How Anna's hummingbirds (*Calypte anna*) fly through upward gusts," J. Exp. Biol. **222**, jeb176263 (2019).
[36]T. Jakobi, D. Kolomenskiy, T. Ikeda, S. Watkins, A. Fisher, H. Liu, and S. Ravi, "Bees with attitude: The effects of directed gusts on flight trajectories," Biol. Open **7**, bio034074 (2018).
[37]M. H. Patel and G. Hancock, "A gust tunnel facility," Report No. 3802 (Aeronautical Research Council Reports and Memoranda, 1976), available at https://reports.aerade.cranfield.ac.uk/handle/1826.2/3082.
[38]D. A. Buell, "An experimental investigation of the velocity fluctuations behind oscillating vanes," Report No. NASA TND-5543 (NASA, 1969).
[39]Y. S. Baik, L. P. Bernal, K. Granlund, and M. V. Ol, "Unsteady force generation and vortex dynamics of pitching and plunging aerofoils," J. Fluid Mech. **709**, 37 (2012).
[40]H. Biler, C. Badrya, and A. R. Jones, "Experimental and computational investigation of transverse gust encounters," AIAA J. **57**, 4608–4622 (2019).
[41]C. Badrya, J. D. Baeder, and A. R. Jones, "Application of prescribed velocity methods to a large-amplitude flat-plate gust encounter," AIAA J. **57**, 3261–3273 (2019).
[42]C. Badrya, H. Biler, A. R. Jones, and J. D. Baeder, "Effect of gust width on flat-plate response in large transverse gust," AIAA J. **59**, 49–64 (2021).
[43]G. Sedky, F. D. Lagor, and A. Jones, "Unsteady aerodynamics of lift regulation during a transverse gust encounter," Phys. Rev. Fluids **5**, 074701 (2020).
[44]G. Sedky, A. R. Jones, and F. D. Lagor, "Lift regulation during transverse gust encounters using a modified Goman–Khrabrov model," AIAA J. **58**, 3788–3798 (2020).
[45]I. Andreu Angulo and H. Babinsky, "Negating gust effects by actively pitching a wing," AIAA Paper No. 2020-1057, 2020.
[46]I. Andreu Angulo and H. Babinsky, "Unsteady modelling of pitching wings for gust mitigation," AIAA Paper No. 2021-1999, 2021.
[47]M. Yu, Z. Wang, and H. Hu, "A high-order spectral difference method for unstructured dynamic grids," Comput. Fluids **48**, 84–97 (2011).
[48]H. T. Huynh, "A flux reconstruction approach to high-order schemes including discontinuous Galerkin methods," AIAA Paper No. 2007-4079, 2007.
[49]Z. Wang and H. Gao, "A unifying lifting collocation penalty formulation including the discontinuous Galerkin, spectral volume/difference methods for conservation laws on mixed grids," J. Comput. Phys. **228**, 8161–8186 (2009).
[50]P. L. Roe, "Approximate Riemann solvers, parameter vectors, and difference schemes," J. Comput. Phys. **43**, 357–372 (1981).
[51]F. Bassi, A. Crivellini, S. Rebay, and M. Savini, "Discontinuous Galerkin solution of the Reynolds-averaged Navier–Stokes and k–ω turbulence model equations," Comput. Fluids **34**, 507–540 (2005).
[52]M. Yu, Z. Wang, and Y. Liu, "On the accuracy and efficiency of discontinuous Galerkin, spectral difference and correction procedure via reconstruction methods," J. Comput. Phys. **259**, 70–95 (2014).
[53]L. Wang and M. Yu, "Comparison of ROW, ESDIRK, and BDF2 for unsteady flows with the high-order flux reconstruction formulation," J. Sci. Comput. **83**, 39 (2020).
[54]P.-O. Persson, J. Bonet, and J. Peraire, "Discontinuous Galerkin solution of the Navier–Stokes equations on deformable domains," Comput. Methods Appl. Mech. Eng. **198**, 1585–1595 (2009).
[55]P. R. Hammer, M. R. Visbal, A. M. Naguib, and M. M. Koochesfahani, "Lift on a steady 2-D symmetric airfoil in viscous uniform shear flow," J. Fluid Mech. **837**, R2 (2018).
[56]E. Laitone, "Wind tunnel tests of wings at Reynolds numbers below 70 000," Exp. Fluids **23**, 405–409 (1997).
[57]H. Liu and K. Kawachi, "A numerical study of undulatory swimming," J. Comput. Phys. **155**, 223–247 (1999).
[58]J. Young and J. C. Lai, "Oscillation frequency and amplitude effects on the wake of a plunging airfoil," AIAA J. **42**, 2042–2052 (2004).
[59]P. R. Hammer, "Computational study of the effect of Reynolds number and motion trajectory asymmetry on the aerodynamics of a pitching airfoil at low Reynolds number," Ph.D. thesis (Michigan State University, 2016).
[60]M. R. Visbal, "High-fidelity simulation of transitional flows past a plunging airfoil," AIAA J. **47**, 2685–2697 (2009).
[61]A. R. Jones, "Gust encounters of rigid wings: Taming the parameter space," Phys. Rev. Fluids **5**, 110513 (2020).
[62]J. Eldredge, C. Wang, and M. Ol, "A computational study of a canonical pitch-up, pitch-down wing maneuver," AIAA Paper No. 2009-3687, 2009.
[63]D. J. Garmann, M. R. Visbal, and P. D. Orkwis, "Three-dimensional flow structure and aerodynamic loading on a revolving wing," Phys. Fluids **25**, 034101 (2013).